Yang et al. *EPJ Quantum Technology* (2023) 10:23
https://doi.org/10.1140/epjqt/s40507-023-00179-w

EPJ Quantum Technology
a SpringerOpen Journal

RESEARCH Open Access

Local oscillator port embedded field enhancement resonator for Rydberg atomic heterodyne technique

Kai Yang[1], Ruiqi Mao[1], Li He[1], Jiawei Yao[2], Jianbing Li[1,3], Zhanshan Sun[1*] and Yunqi Fu[1*]

*Correspondence:
szs199252@163.com;
yunqifu@nudt.edu.cn
[1]College of Electronic Science and Technology, National University of Defense Technology, Changsha, 410073, China
Full list of author information is available at the end of the article

Abstract

Rydberg atom-based sensors using the atomic heterodyne technique demonstrate prominent performance on sensing sensitivity and thus have significant potential for radar, electronic reconnaissance, and communication applications. Here, we propose a local oscillator (LO) embedded field enhancement resonator to improve the sensitivity and integration of Rydberg atomic heterodyne sensors. In this approach, a vapor cell filled with cesium atoms is placed into the resonance structure for electric (E) field measurements. By integrating parallel-plate waveguide (PPWG) antennas and the resonator, the LO signal can be directly guided to the resonator using coaxial cable instead of the use of external antennas radiating through free space, allowing for a more flexible and practical Rydberg atom-based heterodyne technique. Based on the off-resonant Rydberg atomic heterodyne approach, for a radio frequency (RF) signal at 638 MHz, it is found that the sensitivity is 43 μV/cm$\sqrt{\text{Hz}}$ in the absence of the resonator, while in the presence of our resonator, the sensitivity is down to 854.36 nV/cm$\sqrt{\text{Hz}}$, indicating 50 times or 34 dB improvement capacity of the proposed resonator. This type of enhancement resonator is expected to benefit Rydberg atomic heterodyne applications in practical environments.

Keywords: Rydberg atoms; Enhancement resonator; Local oscillator port embedded

1 Introduction

In the past decade, Rydberg atom-based sensors have been an increasingly crucial subset of quantum sensors for radio frequency (RF) electric (E) field measurements thanks to their large electric dipole moments and polarizabilities [1]. The RF signal perturbs the energy of the Rydberg states and causes the shift or splitting of the electromagnetically induced transparency (EIT) spectrum [2], making Rydberg atoms a directly and nondestructively probe medium for E-field. Leveraging the Rydberg-EIT method, the amplitude [3–6], phase [7–9], polarization [10], frequencies [11–13], and angle [14] of the RF field can then be detected. Compared to traditional electronic receivers, the Rydberg atomic sensors offer several superiorities with respect to self-calibration, system international (SI) traceability to Planck's constant, and non-adherence to the Chu limit [15], allowing small and room-temperature vapor cells to operate over multiple octave ranges from kHz to THz

[16–18]. Based on these fascinating properties, various applications began to emerge, including spectrum analyzer [19], microwave frequency comb [20], E-field probes [21, 22], and receivers for communication and radar signals [23–31].

Besides the extension of the application scenarios, a higher sensitivity for E-field measurement is another central pursuit for atomic sensors since the Rydberg atom has the exciting possibility to avoid the internal thermal (Johnson) noise even at room temperature. The measurement sensitivity is highly dependent on the linewidth of EIT, which is typically on the order of 5 to 10 MHz. This is because the minimal detectable field is limited by EIT's spectral resolution, which manifests as an Autler–Townes (AT) splitting in the resonant region or ac Stark shift in the off-resonant region. Researchers have investigated various approaches to improve the measurement sensitivity, such as increasing the number of Rydberg atoms with a ground state repumping laser [32], using three-photon excitation schemes to overcome Doppler mismatch [17, 18], dressing adjacent Rydberg transition by an auxiliary RF field [33–35], driving the critical point of a many-body Rydberg atomic system [36]. One of the most noticeable steps was the introduction of a local oscillator (LO) RF field to the atoms, which is referred to as the Rydberg atomic heterodyne technique [7, 11, 19, 37–40]. It leads to an increase in sensitivity from a few μV/cm$\sqrt{\text{Hz}}$ to 12.5 nV/cm$\sqrt{\text{Hz}}$, an improvement of nearly three orders of magnitude compared to the standard EIT-AT method in resonant regions [38]. The presence of LO fields not only benefits improving the sensing sensitivity but also controls ensembles of Rydberg atoms [7, 14, 19, 29].

The resonant structure can enhance the incident E-field strength at the location of atoms [41, 42], which can further improve the sensing sensitivity in cooperation with the Rydberg atomic heterodyne technique. However, to date, the majority of LO fields were employed via irradiation from free space using antennas. This way of LO loading restricts the application of Rydberg atomic sensors in practical and remote scenarios since the LO field will suffer very severe attenuation in long-range propagation, and the multi-path interference caused by scattering in realistic environments would heavily affect the phase relationship between the LO and signal (SIG) fields, thus deteriorating the sensing sensitivity and even leading to erroneous measurements.

To improve the sensing sensitivity and to further tailor the Rydberg atomic heterodyne technique to the practical environment, we designed a field sensing enhancement resonator that can directly guide the LO signal to the atoms through a coaxial cable and enlarge the localized E-field by integrating the parallel-plate waveguide (PPWG) antennas into the resonator. Inside the resonator, the RF wave propagates between the PPWG and the resonance areas of the resonator via spatial coupling. The LO port reflection coefficient can be adjusted as a trade-off between the field enhancement factor of the entire resonator and the maximum output power of the LO source, depending on the specific application environments. To explore the sensing ability of the E-field under GHz, the focused frequency was chosen as 638 MHz (off-resonant region). The results show that with the presence of the resonator, the measurement sensitivity is down to 854.36 nV/cm$\sqrt{\text{Hz}}$, which is over 50 times improvement than that without the resonator. This type of LO-embedded field enhancement resonator not only improves the sensing sensitivity but also facilitates the practical implication of the Rydberg atomic heterodyne technique.

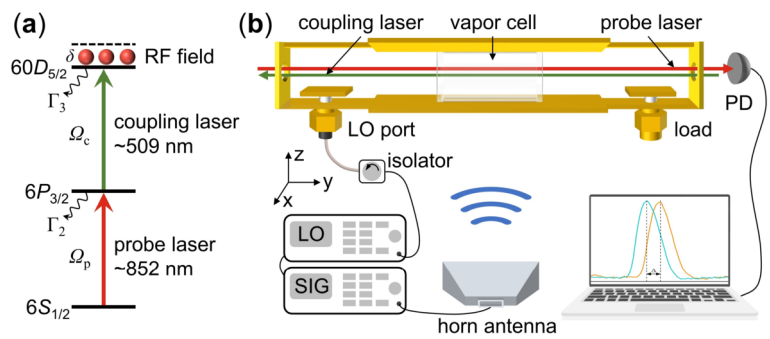

Figure 1 (**a**) Overview of experimental energy diagram. An 852 nm probe laser excites the cesium atoms from the ground state $|6S_{1/2}, F = 4\rangle$ to the intermediate state $|6P_{3/2}, F' = 5\rangle$, and a 509 nm coupling laser drives the atoms from the intermediate state to the Rydberg state $|60D_{5/2}\rangle$. δ is the energy level shift induced by the external RF field according to the ac Stark effect, and Γ_i $(i = 2, 3)$ is the state $|i\rangle$ decay rate. (**b**) Sketch of the experimental setup. A cylindrical vapor cell is embedded into the field-sensing enhancement resonator. The probe light (red) is counter-propagated and overlapped with a coupling light (green) through the optical aperture of the resonator and detected by a photodetector (PD). The LO and SIG fields are generated by two independent SGs that are phase synchronized. The LO signal is guided to the LO port of the resonator via a coaxial cable. An isolator is used between the LO SG and the resonator to absorb the reflected waves from the LO port. Meanwhile, the SIG field is radiated to the resonator through a horn antenna

2 Methods

2.1 Experimental setup

A two-photon Rydberg EIT ladder scheme adopted in the experiments and an overview of the experimental setup are shown in Fig. 1(a) and (b). At room temperature, a cylindrical cesium (^{133}Cs) vapor cell with a length of 20 mm and a diameter of 10 mm is embedded into the field sensing enhancement resonator. A probe laser with a $1/e^2$ beam diameter of 780 μm and a power of 9.3 μW is frequency locked to the D2 transition of $|1\rangle = |6S_{1/2}, F = 4\rangle \rightarrow |2\rangle = |6P_{3/2}, F' = 5\rangle$ via modulated transfer spectroscopy [43]. Meanwhile, a 51.2 mW coupling laser with a $1/e^2$ beam diameter of 1.34 mm is tuned to ~509 nm to further excite the atoms to the Rydberg state $|3\rangle = |60D_{5/2}\rangle$. The probe is counter-propagated and overlapped with the coupling laser inside the vapor cell to minimize Doppler broadening effect and is detected by a photodetector. The LO and SIG fields are generated by two independent signal generators (SGs) that are phase synchronized. The LO signal is guided through the coaxial cable to the LO port of the resonator, with an isolator in the transmission path to absorb reflected waves to protect the instrument. Simultaneously, the SIG signal is radiated to the resonator through free space using a horn antenna. The other port of the resonator absorbs the leakage waves with a matched load to balance the E-field distribution in the resonance area of the resonator. The polarization of the two RF fields is the same as those of the probe and coupling beams and propagates in a vertical direction to the two laser beams.

2.2 Off-resonant Rydberg atomic heterodyne model

To model the off-resonant Rydberg atomic heterodyne system, we consider the three-level system in Fig. 1(a). Under normal resonance conditions, the detuning of the probe and coupling laser $\Delta_p = \Delta_c = 0$, and the $|1\rangle$ and $|2\rangle$ energy level shifts can be ignored since

their low polarizability. The relevant Hamiltonian of our system can be written as [37]

$$H = \frac{\hbar}{2}\begin{pmatrix} 0 & \Omega_{\mathrm{p}} & 0 \\ \Omega_{\mathrm{p}} & 0 & \Omega_{\mathrm{c}} \\ 0 & \Omega_{\mathrm{c}} & \delta \end{pmatrix}, \tag{1}$$

where $\hbar$ is the reduced Planck's constant, Ω_{p} and Ω_{c} are the Rabi frequencies associated with the probe and coupling lasers, respectively, and $\delta = -(1/2)\alpha\langle E_{\mathrm{tot}}^2\rangle$ is the spectrum shift caused by the ac Stark effect, where α is the dc polarizability, and $\langle E_{\mathrm{tot}}^2\rangle$ is the average value of the square of the E-field. The Rydberg atoms have a very large polarizability, which makes them more sensitive to the external RF field. Considering the spontaneous emission, the dynamics of our system is governed by the following master equation

$$\dot{\rho} = \frac{i}{\hbar}[\rho, H] + \mathcal{L}. \tag{2}$$

Where the second term is given by

$$\mathcal{L} = \begin{pmatrix} \Gamma_2\rho_{22} & -\gamma_{12}\rho_{12} & -\gamma_{13}\rho_{13} \\ -\gamma_{21}\rho_{21} & \Gamma_3\rho_{33} - \Gamma_2\rho_{22} & -\gamma_{23}\rho_{23} \\ -\gamma_{31}\rho_{31} & -\gamma_{32}\rho_{32} & -\Gamma_3\rho_{33} \end{pmatrix}, \tag{3}$$

Where $\gamma_{ij} = (\Gamma_i + \Gamma_j)/2$ and $\Gamma_{i,j}$ are the transition decay rates (Fig. 1(a)). Here we have ignored the Doppler broadening effect for simplicity. The steady-state solution of the system density matrix can be obtained when $\dot{\rho} = 0$ in Equation (2), and the susceptibility is further obtained

$$\chi_{21} = -\frac{2N_0\mu_{12}^2}{\varepsilon_0\hbar\Omega_p}\rho_{21}, \tag{4}$$

where N_0 is the total density of atoms, μ_{12} is the transition dipole moment between $|2\rangle$ and $|1\rangle$, and ε_0 is the permittivity in vacuum. After that, we can obtain the probe beam power measured on the photodetector, which is calculated as $P(t) = P_0\exp(-\beta L)$, where P_0 is the incident power to the cell, L is the length of the cell, $\beta = 2\pi\,\mathrm{Im}[\chi(t)]/\lambda_{\mathrm{p}}$ is the Beer's absorption coefficient for the probe laser, and λ_{p} is the wavelength of the probe laser.

When it comes to the Rydberg atomic heterodyne technique, the total E-field will become $\mathbf{E}_{\mathrm{LO}}+\mathbf{E}_{\mathrm{SIG}}$, and the Stark shift induced by the total E-field is $\delta = -1/2\alpha(\mathbf{E}_{\mathrm{LO}} + \mathbf{E}_{\mathrm{SIG}})^2$. Here, we set the LO and SIG fields to be phase synchronous and let $\varphi_{\mathrm{LO}} = \varphi_{\mathrm{SIG}}$. Taking a time average, we obtain [17]

$$\overline{\delta} = \overline{\delta_0} - \frac{1}{2}\alpha\left[E_{\mathrm{LO}}E_{\mathrm{SIG}}\cos(\Delta\omega * t)\right]. \tag{5}$$

Where $\Delta\omega$ represents the beat-note frequency between the LO and SIG fields, and $\overline{\delta_0} = -1/4\alpha(E_{\mathrm{LO}}^2 + E_{\mathrm{SIG}}^2)$ is the average ac Stark shift caused by the LO and SIG fields. From Equation (5), we can see that the energy level shift is modulated by the beat-note frequency. Furthermore, the magnitude of the SIG field can be extracted by measuring the beat-note frequency component of the probe laser.

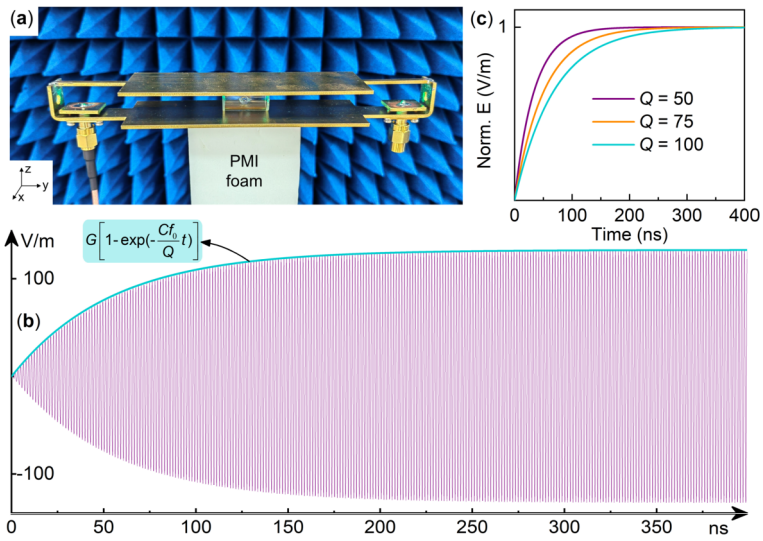

Figure 2 Field sensing enhancement resonator and the time dependent E-field response. (**a**) The resonator used in the experiments. A cylindrical cesium vapor cell is placed inside the resonator, and the entire structure is supported by PMI foam to reduce scattering. The resonator has two SMA ports. One is used as the LO signal input port, and the other is terminated to a 50 Ω load. (**b**) The purple curve is the simulated time dependent E-field strength for a probe located at the center of the resonator. The blue curve corresponds to the theoretical fit from Equation (6) with $G = 129.5$, $f_0 = 638$ MHz, $C = 2.3$, and $Q = 79.16$. (**c**) Normalized theoretical time dependent E-field response for different Q values of 50, 75, and 100. For a given incident wave frequency, the higher the Q value, the longer the time is required to reach a steady state

3 Results

The LO-embedded field sensing enhancement resonator used in the experiments is shown in Fig. 2(a). The resonator is made of copper plates with a thickness of 1.5 mm for higher mechanical strength and has two symmetrical Sub-Miniature-A (SMA) ports. One port is used to feed the LO signal into the resonance area, and the other port is terminated to a 50 Ω load. The resonator is supported by polymethacrylimide (PMI) foam with a relative permittivity of ∼1.1 to minimize scattering from the ambient surroundings. It has been shown that the resonant structure has a polarization selective behavior [41, 42, 44]. In detail, if the E-field is perpendicular to the plane of the resonator ($\vec{E} \parallel \vec{z}$), it will have the maximum enhancement factor, on the other hand, if the E-field is parallel to the plane of the resonator ($\vec{E} \perp \vec{z}$), then the resonance response is negligible. The maximum response area of the whole structure is the gap between the upper and lower parallel plates, and when the vapor cell is embedded into the gap, the atoms will be exposed to the enhanced field. The resonance frequency of the resonator depends mainly on the loop size as well as the area and separation of the gap [44]. The resonator used in our experiments is simulated by a commercial finite-element simulator with a resonance frequency near 638 MHz.

To evaluate the steady time of the resonator, we simulated the time dependent E-field response at the center of the resonator, as shown in Fig. 2(b). The E-field between the gap can be expressed as [45]

$$E(t) = G\left[1 - \exp\left(-\frac{Cf_0}{Q}t\right)\right], \tag{6}$$

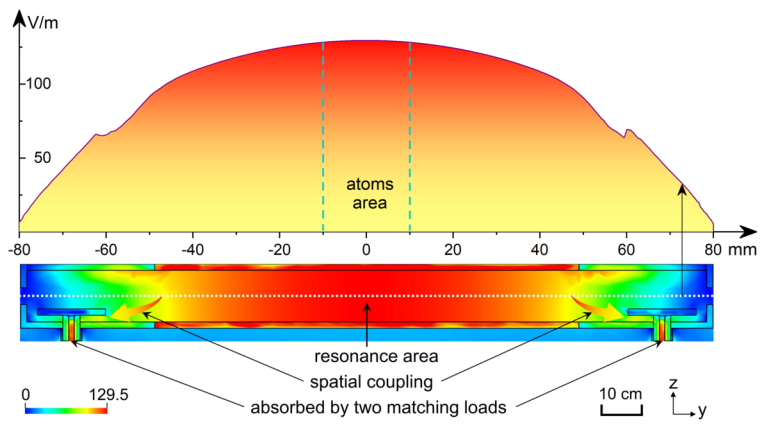

Figure 3 Simulated E-field distribution for a 638 MHz incident source. The energy captured by the resonator, in addition to resonating between the gap, is absorbed by matched loads connected by two symmetrical PPWG antennas through spatial coupling. The upper panel shows the E-field distribution along the optical beam path (white dashed line in the lower panel), with the vertical dashed lines delineating the vapor cell location. The black lines delineate the copper plate of the resonator

where G is the enhancement factor of the resonator, C is a constant determined by the resonator structure, f_0 is the frequency of the incident wave, $Q = f_0/BW$ is the quality factor of the resonator, and BW is the 3 dB bandwidth of the magnitude of the E-field. Note that the E-field between the gap is determined by a steady-state response for the external excitation and a transient response that decays exponentially with time. We define $\tau_0 = Q/Cf_0$ as the relaxation time for the transient response to decay to $1/e$. In our simulation, the relaxation time τ_0 of our resonator is about 53.9 ns, less than the Rydberg atomic decoherence time, which is approximately on the order of microseconds [19, 25]. For a given incident wave frequency, τ_0 is proportional to Q, as shown in Fig. 2(c). Thus, for time-varying applications, Q cannot be infinitely large to ensure that τ_0 is less than the SIG field retention time.

Besides the time dependent E-field response, we also investigated the steady-state E-field distribution of the resonator. Figure 3 illustrates the numerical results for a 638 MHz plane wave irradiating on the resonator. The lower half of the figure shows a heatmap of the E-field distribution in the resonant, and the upper half shows the E-field distribution along the optical beam path (white dashed line in the lower half). This plane wave has an amplitude of 1 V/m and is linearly polarized along the $\vec{z}$ direction. Due to the discontinuity of boundary conditions, the E-field inside the resonator is inhomogeneous along the optical beam path, the Rydberg EIT line is a combination of the probe beam absorption through many discrete thin segments, and thus this disharmony of the E-field would broaden the atomic spectral signatures and therefore deteriorate the measurement accuracy [22]. In our design, we extend the length of the resonance area to eliminate this inhomogeneity among the area of measurement. Specifically, the E-field intensity fluctuates about 1% in the optically interrogated atomic detection region. Future work will explore other ways to improve the E-field uniformity, such as varying the gap size along the optical beam path.

The response of the device to the E-field can be analyzed from the standpoint of the LO and SIG fields, respectively. From the LO perspective, the LO signal can be guided to the resonator via a coaxial cable and then converted into a spatial electromagnetic (EM) wave by the PPWG antenna, which shares a common floor with the resonator. Subsequently, a

fraction of the LO signal leaks into the resonance area through spatial coupling as the LO field of the atoms. From the SIG perspective, the EM energy is mainly resonating between the gap, while a minority is absorbed by the matching loads, which are connected by two symmetrical PPWG antennas via spatial coupling (there is an isolator between the LO port and the SG).

The absorption of the loads leads to a reduction of EM energy in the resonance area, which further leads to a decrease of the enhancement factor G. From an energy perspective, the relationship between G and the LO port reflection coefficient S_{11} can be expressed as

$$\left(\frac{G}{G_{\max}}\right)^2 = \eta |S_{11}|^2, \tag{7}$$

where $G_{\max}$ is the maximum enhancement factor when there are no matched loads on the two ports. $(G/G_{\max})^2$ represents the ratio of the EM energy preserved in the resonance area to that captured through free space while $|S_{11}|^2$ represents the ratio of the reflected EM energy to the total input EM energy of the LO port. Considering that the resonator is a passive structure, according to the reciprocity principle, there exists a scaling factor between these two ratios, denoted by η. Here η is a constant less than 1 because of the conductor loss and radiation loss. In practice, the LO port reflection coefficient S_{11} can be adjusted as a tradeoff between the field enhancement factor G and the maximum output power of the LO source. Note that a poor S_{11} at the LO port is tolerated since the resonator will also enhance the LO signal.

Figure 4 shows the three EIT spectral signals as a function of the coupling laser detuning. In this experiment, only the SIG source was turned on with its frequency set to 638 MHz, and the SG output power was varied during the experiment. The black solid curve is the reference EIT, which is obtained by turning off the SG. When the RF field is turned on, the EIT spectrum will shift to the right, which can be explained by the ac Stark effect. In addition to the shift, the EIT spectrum undergoes a broadening due to the unintentional polarization introduced by the scattering of the components on the optical table. Subsequently, the magnetic substates of $nD_{5/2}$ begin to split thanks to the different angular matric elements [22]. The purple dashed curve shows the EIT spectrum without our resonator, with a SG output power of 17 dBm. By applying the resonator, the required SG output power to obtain the same EIT shift (13.9 MHz) drops to −17 dBm, shown as the orange solid curve, indicating that the resonator enhances the E-field by a factor of $\sqrt{10^{34/10}} = 50.12$. Note that the enhancement factor is determined by comparing the SG output power corresponding to the same EIT spectrum with and without the resonator, where the polarizability is eliminated during the comparison. Therefore, the magnetic substates have almost no effect on the enhancement factor.

Figure 5 demonstrates the experimental and numerical frequency and polarization response of the resonator. Similar to the enhancement factor determination method in Fig. 4, we obtained the experimental enhancement data for the resonator in Fig. 5(a) under different RF detunings. The numerical results in Fig. 5(a) are acquired without considering ambient factors. The data in Fig. 5(a) can be classified into two categories: Case 1. Enhancement factors under atomic heterodyne conditions which is obtained by terminating the two SMA ports with loads. Case 2. Maximum enhancement factors which are obtained by open-loading these two ports. It can be seen that the measured results have lower and

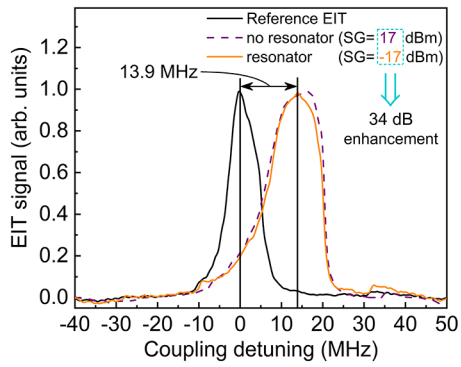

Figure 4 Measured EIT signals versus coupling laser detuning. When there is no RF field, we obtain a reference EIT with a peak at 0 MHz coupling detuning. Once the atoms are exposed to the RF field at 638 MHz, the EIT spectrum shifts to the right according to the ac Stark effect. In the absence of the resonator, the output power of the SG is 17 dBm with a Stark shift of 13.9 MHz, while in the presence of the resonator, the output power drops to −17 dBm resulting in the same Stark shift of the EIT spectrum

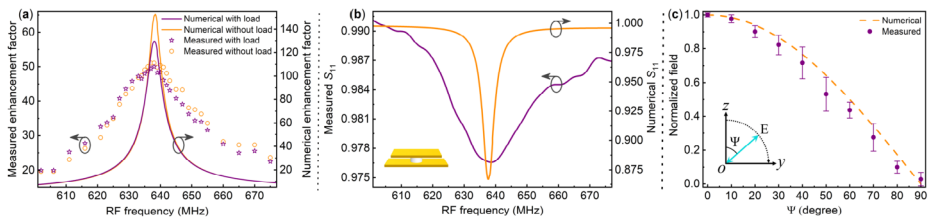

Figure 5 Measured and simulated frequency and polarization response of the resonator. (**a**) Enhancement factor versus RF field frequency. There are two cases in these data, one is the two ports of the resonator are terminated with loads, and the other case is that these two ports are no-loaded. (**b**) S_{11} of the LO port versus RF field frequency when the other port is terminated with a load. (**c**) Normalized polarization response at 638 MHz for atomic heterodyne conditions by rotating the SIG antenna. The error bars correspond to the standard deviation of three datasets

Table 1 The quality factor Q and loss coefficient η at the resonance frequency of 638 MHz

	Enhancement factor G		3 dB bandwidth BW (MHz)		Quality factor Q		Reflect coefficient S_{11}		Loss coefficient η	
	Num.	Exp.	Num.	Exp.	Num.	Exp.	Num.	Exp.	Num.	Exp.
Case 1	129.49	50.12	8.06	54.25	79.16	11.76	0.87	0.98	0.95	0.99
Case 2	152.56	51.17	6.76	57.59	94.38	11.08				

wider peaks compared to the numerical results. This broadening trend can also observe in the measured LO port reflection coefficient (S_{11}), as shown in Fig. 5(b). The high S_{11} level means that only a relatively minor portion of the energy is injected into the resonator. It should be pointed out that since the resonator also enhances the LO signal, only a moderate amount of energy is required to satisfy the LO field intensity.

Generally, the performance of the resonant structure can be evaluated by the quality factor Q. The calculation of the quality factor Q and the loss coefficient η with part of the experimental and numerical data in Fig. 5(a) and (b) is given in Table 1. In both cases, the measured Q deteriorates seriously, and it decreases more dramatically for case 2. This discrepancy is roughly attributed to three reasons. First, the conductivity of the inner surface of the vapor cell is nonzero thanks to the adsorption of alkali-metal atoms [16]. This E-field screening effect will worsen the enhancement factor when embedding a vapor cell into a resonant structure. Second, in addition to the resonator itself, scattering from the surrounding can also change the E-field distribution at atoms position. The multi-path

effect may also reduce the enhancement factor. Third, the losses (metallic and dielectric) of the resonator and variances in the fabricated dimensions may also lead to a reduction in the enhancement factor. Both the experimental and numerical η are close to 1, while the measured η is larger. This difference could be attributed to the fact that the loads are not completely absorbed, and the structure is not perfectly grounded during the measurement. Besides, for a constant Q, the enhancement factor and the 3 dB bandwidth are inversely proportional to each other. Similar to the selection of the relaxation time τ_0, there may be a trade-off between the enhancement factor and the response bandwidth in a particular implementation. Specifically, the 3 dB bandwidth of our resonator is much larger than the EIT linewidth, which is sufficient for Rydberg atomic heterodyne applications [19].

In addition to investigating the frequency selectivity of the resonator, we also examined its polarization selectivity. In this experiment, by rotating the horn antenna (Fig. 1(b)), we varied the polarization of the SIG field at a fixed SG output power of −40 dBm. Figure 5(c) shows the normalized experimental and numerical results as the SIG E-field is rotated from z-polarization ($\Psi = 0°$) to y-polarization ($\Psi = 90°$). The mismatching between these results might be attributed to multi-path effects and the inaccuracy of antenna rotation. These results indicate that the resonator is highly polarization selective, which is determined by the configuration of the resonator.

To verify the benefits of our resonator in terms of the LO field integration and SIG field enhancement, we compared the E-field sensing performance under the conditions with or without the resonator for the atomic heterodyne scenario. In the case with the resonator, the LO field is applied to the atoms by the LO port of the resonator, while in the case without the resonator, the LO field is radiated through the same antenna together with the SIG field using a power splitter. In order to acquire an accurate enhancement factor under atomic heterodyne conditions, it is essential to guarantee that the LO field strength is the same with and without the resonator. Therefore, we turned off the SIG field first and obtained the EIT spectrum shifts versus the power fed to the antenna or the LO port of the resonator at 638 MHz, as shown in Fig. 6. Regardless of where the LO signal is fed from, there is a clear linear relationship between the spectrum shift and the SG output power. This linear relationship can be explained by the ac Stark effect, where $\delta \propto E^2$, considering that the SG output power is proportional to the square of the E-field strength.

In the absence of the resonator, the SIG signal amplitude is fixed at −40 dBm, and the optimized LO field strength can be obtained by tuning the LO signal amplitude for the maximum spectrum analyzer output. In this case, the optimized LO signal value is 13.183 mW, inducing a spectrum shift of 3.31 MHz, as shown by the vertical black dashed line in Fig. 6. In our experiments, the lasers and RF fields are linearly polarized and parallel to each other, leading to a near-degeneracy between the $m_j = 1/2$, 3/2, and 5/2 magnetic substates of the $60D_J$ levels in weak E-fields. Therefore, the overall EIT spectral shift is primarily evident in the $m_j = 1/2$ magnetic substate. By employing the Alkali Rydberg Calculator (ARC) package [46] and applying the Floquet theory [47], we can calculate the polarizability $\alpha(2\pi \times 638\ \text{MHz})$ of the $|60D_{5/2}, m_j = 1/2\rangle$ state as −5.38 GHz·cm^2/V^2, and subsequently, we can derive the E-field strength as 4.91 V/m at a Stark shift of 3.31 MHz. In the presence of the resonator, this spectrum shift corresponds to a LO signal of 0.0286 mW. Note that despite the poor match of the LO port, the LO power required when leveraging the resonator is only 0.0286/13.183 = 0.217% relative to that without the resonator. This is

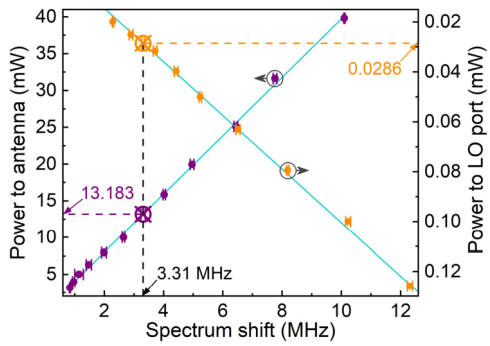

Figure 6 The EIT spectrum shifts versus the SG output power fed to the antenna or the LO port of the resonator at 638 MHz. These data were obtained in the presence of the LO field only and show a clear linear relationship that could be used to infer the E-field strength at the atoms position for different SG output powers. The optimized LO field strength of 4.91 V/m induces a spectrum shift of 3.31 MHz. This shift corresponds to an SG output power of 13.183 mW (when it is fed to the antenna) and 0.0286 mW (when it is fed to the LO port of the resonator). The error bars correspond to the standard deviation of three datasets

because the resonator avoids spatial radiation attenuation and has an enhancement effect on the LO signal. These benefits are even more substantial for remote sensing applications, where spatial radiation attenuation is significant.

To explore the sensitivity of the atomic heterodyne approach under GHz, we set the LO frequency to 638 MHz and the SIG frequency to 638.01 MHz. Once the coupling laser is fixed at an optimal operating point, the probe laser intensity will fluctuate at a beat-note frequency of 10 kHz. Then, we measured the intensity of the photodetector output signal with a spectrum analyzer with a resolution bandwidth of 1 Hz. Figure 7 shows the beat-note intensity with and without the resonator at different SIG field strengths and indicates that the sensing capability improves more than 34 dB. The error bars correspond to the standard deviation of five datasets, reflecting the instability of the laser power and laser frequency. The strength of the received beat-note signal is approximately linearly proportional to the strength of the applied SIG field. In theory, the sensitivity is defined as the minimum detectable power when the signal-noise ratio (SNR) is downs to 1. Here we obtained the minimum power by finding the intersections of the linear response curves and the spectrum analyzer noise floor. Following this criterion, we obtain the measured sensitivities of 854.36 nV/cm$\sqrt{\text{Hz}}$ and 43 μV/cm$\sqrt{\text{Hz}}$ with and without the resonator, respectively. Comparing these two sets of results, we see that the resonator does show an E-field enhancement effect over 50 times. Consequently, this type of resonator can be used to substantially improve the sensing sensitivity of the Rydberg atom-based atomic heterodyne sensors.

4 Discussion

According to the way in which the SIG field enters the Rydberg atoms, atomic sensors can be broadly classified into two categories, injected sensors and open sensors. Injected sensors, as mentioned in Reference [19], the SIG field is captured by an electronic antenna and guided into a chamber filled with alkali metal atoms. This injection method benefits the loading of LO field and can improve sensing sensitivity by the usage of high gain antenna and preamplification. However, the microwave transmission path in injected sensors introduces additional undesired noise to the atoms, which means that it is impossible

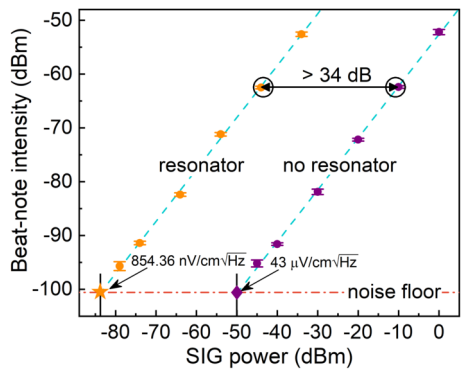

Figure 7 The beat-note intensity as a function of the SG output power of the SIG field in the presence and absence of the resonator. The spectrum analyzer output signal showed a linear relationship with the SIG field strength. The sensing sensitivity with and without the resonator are 854.36 nV/cm$\sqrt{\mathrm{Hz}}$ and 43 μV/cm$\sqrt{\mathrm{Hz}}$, respectively, indicating an E-field enhancement factor of over 50 with the resonator. The error bars correspond to the standard deviation of five datasets

Table 2 Performance comparison

References	Center frequency	Electrical size	Enhancement factor	LO port
[31]	19.629 GHz	3.273 λ	∼2.5	Yes
[41]	1.309 GHz	0.096 λ	100	No
[42]	4.35 GHz	∼0.435 λ	16.2	No
This work	638 MHz	0.342 λ	50.12	Yes

to break the thermal noise limit, arguably one of the most exciting advantages of atomic sensors over traditional electronic receivers. In contrast, open sensors allow the SIG field to be irradiated directly into the vapor cell exposed [7, 37] or encased in the structure [31, 41, 42]. When it comes to the fiber-coupled vapor cells [21], open sensors are more flexible in practical applications. Moreover, the sensing sensitivity of open sensors can be further improved by additional devices, for example, by focusing the incident wave with a parabolic surface.

To illustrate the advantage and novelty of this work, the comparison between our resonator and other reported enhancement structures for open-type Rydberg atomic sensors is listed in Table 2. Compared with the work in References [41] and [42], we provide a more flexible way to construct the atomic heterodyne configuration, which is critical for amplitude and phase measurements of the E-field. Furthermore, it shows that our resonator has clear advantages in terms of enhancement factor and electrical size compared to the structure in Reference [31]. In addition, the E-field uniformity in the atomic interrogation region is taken into account in our resonator, which has not been mentioned in other reports. In our design, the E-field inhomogeneity is eliminated by extending the length of the resonance region. This approach worsens the enhancement factor and electrical size, thus the overall performance of the proposed design can get further optimized by using other reasonable E-field uniformity methods.

5 Conclusion

In summary, we have demonstrated a LO embedded field enhancement resonator for Rydberg atomic heterodyne applications. This integrated resonator facilitates substantial flexibility and improves the sensitivity of Rydberg atom-based heterodyne sensors. In this

study, we investigated the relationship between the enhancement factor and the LO port reflection coefficient and demonstrated a power enhancement gain of over 34 dB. In the off-resonant frequency region at 638 MHz, the atomic heterodyne measurement sensitivity is improved from 43 μV/cm$\sqrt{\text{Hz}}$ to 854.36 nV/cm$\sqrt{\text{Hz}}$ with the presence of the resonator, which is over 50 times enhancement. In principle, the operating frequency can be extended to arbitrary frequencies, and the enhancement factor can be increased by optimizing the structure of the resonator. Rydberg atomic heterodyne sensors incorporated with this type of resonator will pave the way for practical scenarios.

Funding
This work was supported by the National Natural Science Foundation of China (NSFC) (Grant No. 12104509), and the Research Project of National University of Defense Technology (Grant No. ZK22-59).

Availability of data and materials
The datasets used or analysed during the current study are available from the corresponding author on reasonable request.

Declarations

Ethics approval and consent to participate
Not applicable.

Consent for publication
Not applicable.

Competing interests
The authors declare no competing interests.

Author contributions
KY, RM and YF conceived the idea and the scheme. KY and JY derived the theoretical framework. KY and LH performed the measurements. KY implemented numerical simulations and was a major contributor in writing the manuscript. ZS, JL and YF contributed to the comment and revision of the manuscript. All authors read and approved the final manuscript.

Author details
[1]College of Electronic Science and Technology, National University of Defense Technology, Changsha, 410073, China. [2]Northwest Institute of Nuclear Technology, Xi'an, 710024, China. [3]State Key Laboratory of Complex Electromagnetic Environmental Effects on Electronics and Information System, National University of Defense Technology, Changsha, 410073, China.

Received: 9 March 2023 Accepted: 4 June 2023 Published online: 26 June 2023

References

1. Gallagher TF. Rydberg Atoms. Cambridge: Cambridge University Press; 1994.
2. Mohapatra AK, Jackson TR, Adams CS. Phys Rev Lett. 2007;98:113003.
3. Sedlacek JA, Schwettmann A, Kübler H, Löw R, Pfau T, Shaffer JP. Nat Phys. 2012;8:819–24.
4. Holloway CL, Gordon JA, Jefferts S, Schwarzkopf A, Anderson DA, Miller SA, Thaicharoen N, Raithel G. IEEE Trans Antennas Propag. 2014;62:6169–82.
5. Paradis E, Raithel G, Anderson DA. Phys Rev A. 2019;100:022126.
6. Holloway CL, Simons MT, Kautz MD, Haddab AH, Gordon JA, Crowley TP. Appl Phys Lett. 2018;113:094101.
7. Simons MT, Haddab AH, Gordon JA, Holloway CL. Appl Phys Lett. 2019;114:114101.
8. Anderson DA, Sapiro RE, Gonçalves LF, Cardman R, Raithel G. Phys Rev Appl. 2022;17:044020.
9. Jia FD, Zhang HY, Liu XB, Mei J, Yu YH, Lin ZQ, Dong HY, Liu Y, Zhang J, Xie F. J Phys B, At Mol Opt Phys. 2021;54:165501.
10. Sedlacek JA, Schwettmann A, Kübler H, Shaffer JP. Phys Rev Lett. 2013;111:063001.
11. Gordon JA, Simons MT, Haddab AH, Holloway CL. AIP Adv. 2019;9:045030.
12. Bussey LW, Winterburn A, Menchetti M, Burton F, Whitley T. J Lightwave Technol. 2021;39:7813–20
13. Liu ZK, Zhang LH, Liu B, Zhang ZY, Guo GC, Ding DS, Shi BS. Nat Commun. 2022;13:1997.
14. Robinson AK, Prajapati N, Senic D, Simons MT, Holloway CL. Appl Phys Lett. 2021;118:114001.
15. Chu LJ. J Appl Phys. 1948;19:1163.
16. Jau YY, Carter T. Phys Rev Appl. 2020;13:054034.
17. Liu B, Zhang LH, Liu ZK, Zhang ZY, Zhu ZH, Gao W, Guo GC, Ding DS, Shi BS. Phys Rev Appl. 2022;18:014045.
18. Chen SY, Reed DJ, MacKellar AR, Downes LA, Almuhawish NFA, Jamieson MJ, Adams CS, Weatherill KJ. Optica. 2022;9:485–91.
19. Meyer DH, Kunz PD, Cox KC. Phys Rev Appl. 2021;15:014053.
20. Zhang LH, Liu ZK, Liu B, Zhang ZY, Guo GC, Ding DS, Shi BS. Phys Rev Appl. 2022;18:014033.
21. Simons MT, Gordon JA, Holloway CL. Appl Opt. 2018;57(22):6456–60.

22. Anderson DA, Sapiro RE, Raithel G. IEEE Trans Antennas Propag. 2021;69:5931–41.
23. Holloway CL, Simons MT, Haddab AH, Gordon JA, Voran SD. IEEE Antennas Propag Mag. 2021;63:63–76.
24. Yang K, Sun ZS, Mao RQ, Lin Y, Liu Y, An Q, Fu YQ. Chin Opt Lett. 2022;20:081203.
25. Anderson DA, Sapiro RE, Raithel G. IEEE Trans Antennas Propag. 2021;69:2455–62.
26. Otto JS, Hunter MK, Kjærgaard N, Deb AB. J Appl Phys. 2021;129:154503.
27. Cox KC, Meyer DH, Fatemi FK, Kunz PD. Phys Rev Lett. 2018;121:110502.
28. Meyer DH, Cox KC, Fatemi FK, Kunz PD. Appl Phys Lett. 2018;112:211108.
29. Holloway CL, Simons MT, Gordon JA, Novotny D. IEEE Antennas Wirel Propag Lett. 2019;18:1853–7.
30. Yang K, Mao RQ, An Q, Li JB, Sun ZS, Fu YQ. Sens Actuators A, Phys. 2023;351:114167.
31. Simons MT, Haddab AH, Gordon JA, Novotny D, Holloway CL. IEEE Access. 2019;7:164975–85.
32. Prajapati N, Robinson AK, Berweger S, Simons MT, Artusio-Glimpse AB, Holloway CL. Appl Phys Lett. 2021;119:214001.
33. Simons MT, Artusio-Glimpse AB, Holloway CL, Imhof E, Jefferts SR, Wyllie R, Sawyer BC, Walker TG. Phys Rev A. 2021;104:032824.
34. Jia FD, Liu XB, Mei J, Yu YH, Zhang HY, Lin ZQ, Dong HY, Zhang J, Xie F, Zhong ZP. Phys Rev A. 2021;103:063113.
35. Yao JW, An Q, Zhou YL, Yang K, Wu FC, Fu YQ. Opt Lett. 2022;47(20):5256–9.
36. Ding DS, Liu ZK, Shi BS, Guo GC, Mølmer K, Adams CS. Nat Phys. 2022;18:1447–52.
37. Jing MY, Hu Y, Ma J, Zhang H, Zhang LJ, Xiao LT, Jia ST. Nat Phys. 2020;16:911–5.
38. Cai MH, Xu ZS, You SH, Liu HP. Photonics. 2022;9:250.
39. Hu J, Li H, Song R, Bai J, Jiao Y, Zhao J, Jia S. Appl Phys Lett. 2022;121:014002.
40. You SH, Cai MH, Zhang SS, Xu ZS, Liu HP. Opt Express. 2022;30:16619–29.
41. Holloway CL, Prajapati N, Artusio-Glimpse AB, Berweger S, Simons MT, Kasahara Y, Alù A, Ziolkowski RW. Appl Phys Lett. 2022;120:204001.
42. Anderson DA, Paradis EG, Raithel G. Appl Phys Lett. 2018;113:073501.
43. Yang K, Mao RQ, An Q, Sun ZS, Fu YQ. Chin Opt Lett. 2023;21:021407.
44. Sydoruk O, Tatartschuk E, Shamonina E, Solymar L. J Appl Phys. 2009;105:014903.
45. Guo YF, Zhang ZC, Fu CJ. High Power Laser Part Beams. 2011;23:073104
46. Šibali´c N, Pritchard J, Adams C, Weatherill K. Comput Phys Commun. 2017;220:319.
47. Jiao Y, Hao L, Han X, Bai S, Raithel G, Zhao J, Jia S. Phys Rev Appl. 2017;8:014028.

Publisher's Note